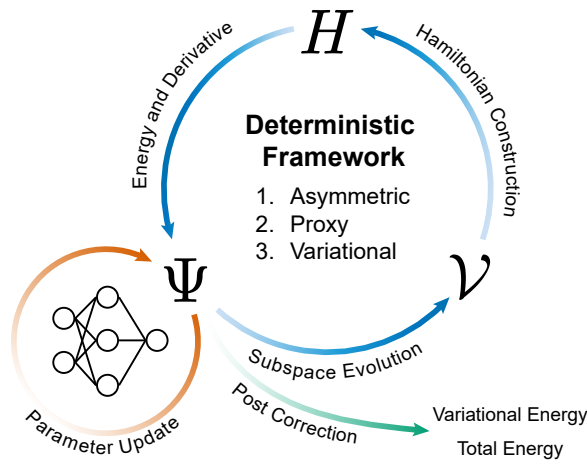


# A Deterministic Framework for Neural Network Quantum States in Quantum Chemistry

Zheng Che<sup>\*1</sup>

<sup>1</sup>*Hefei National Research Center for Physical Sciences at the Microscale, University of Science and Technology of China, Hefei 230026, China*



## Abstract

Stochastic optimization of Neural Network Quantum States (NQS) in discrete Fock spaces is limited by sampling variance and slow mixing. We present a deterministic framework that optimizes a neural backflow ansatz within dynamically adaptive configuration subspaces, corrected by second-order perturbation theory. This approach eliminates Monte Carlo noise and, through a hybrid CPU-GPU implementation, exhibits sub-linear scaling with respect to subspace size. Benchmarks on bond dissociation in  $\text{H}_2\text{O}$  and  $\text{N}_2$ , and the strongly correlated chromium dimer ( $\text{Cr}_2$ ), validate the method's accuracy and stability in large Hilbert spaces.

<sup>\*</sup>Corresponding author: wsmxcz@gmail.com

# 1 Introduction

Solving the electronic Schrödinger equation within a finite basis set remains a fundamental challenge in ab initio quantum chemistry. While Full Configuration Interaction (FCI) offers an exact solution, its exponential scaling necessitates approximations[1–3]. Selected Configuration Interaction (sCI) methods address this by iteratively constructing a variational subspace of dominant Slater configurations[4–7], whereas methods like Coupled Cluster (CC)[8, 9] and Matrix Product States (MPS)[10, 11] seek compact representations via non-linear ansätze. Recently, Neural Network Quantum States (NQS) have been proposed as a flexible alternative, leveraging deep neural networks to parameterize complex many-body wavefunctions[12–18].

However, the application of NQS to second-quantized chemistry is limited by optimization challenges. Conventional Variational Monte Carlo (VMC) relies on Markov Chain Monte Carlo (MCMC) to sample the Hilbert space. Unlike continuous real-space formulations[18–20], the probability distribution of molecular wavefunctions in Fock space is discrete, sparse, and often multimodal. MCMC sampling in this regime suffers from slow mixing and high variance[14, 21–23], obscuring the intrinsic representational capacity of the neural ansatz. While autoregressive architectures circumvent MCMC bottlenecks via direct i.i.d. sampling, they necessitate a rigid ordering that can structurally constrain symmetry-respecting ansätze and introduce an artificial "causality" into the static wavefunction. Furthermore, even with unbiased samples, the variance of stochastic energy estimators remains high for the sparse and multimodal distributions typical of strongly correlated systems, leaving the optimization challenge fundamentally unresolved[23–27].

To overcome these limitations, we present a deterministic optimization framework for NQS in molecular systems. Building on recent deterministic strategies[21, 22, 28], we treat the neural network as a deterministic generator of amplitudes rather than a stochastic sampler. By projecting the ansatz onto a dynamically adaptive configuration subspace, stochastic estimation is replaced by exact summation. This reformulation converts the problem into the minimization of an energy functional defined by an effective Hamiltonian. While the framework unifies several optimization objectives, we identify a protocol combining strict variational optimization within the adaptive subspace and a post-hoc second-order Epstein-Nesbet perturbation theory (PT2) correction as the most robust strategy for recovering both static and dynamic correlations.

This approach differs fundamentally from sCI and Machine Learning-enhanced CI (MLCI) methods[28, 29]. Although sCI and MLCI also exploit Hilbert space sparsity, they rely on iterative linear algebra solvers to determine wavefunction coefficients. In contrast, our framework solves a non-linear optimization problem where amplitudes are directly parameterized by the neural network weights. This eliminates the diagonalization step and provides a noise-free environment to rigorously evaluate the compactness and accuracy of neural ansätze.

We evaluate this framework using a Multi-Layer Perceptron (MLP) backflow ansatz without pre-training and parameter fine-tuning. Implemented via a hybrid CPU-GPU algorithm, the method achieves chemical accuracy for the bond dissociation of H<sub>2</sub>O and N<sub>2</sub> in the cc-pVDZ basis set. Notably, for the strongly correlated chromium dimer (Cr<sub>2</sub>), the Variational+PT2 protocol yields total energies consistent with high-precision benchmarks, demonstrating applicability to large Hilbert spaces where stochastic optimization typically struggles.

The paper is organized as follows. Section 2 details the theoretical framework, analyzing the effective Hamiltonians and the Variational+PT2 protocol. Section 3 describes the hybrid computational implementation and subspace evolution algorithms. Section 4 presents numerical benchmarks, and Section 5 concludes the work.

## 2 Theory

We present the deterministic optimization framework for the time-independent electronic Schrödinger equation. We first define the Fock space notation and the geometry of the configuration sets (section 2.1), followed by the formulation of the Neural Network Quantum States (section 2.2). Subsequently, we define the deterministic energy objectives (section 2.3) and outline the self-consistent optimization procedure (section 2.4).

### 2.1 Framework and Notation

We consider the fermionic Fock space restricted to the sector with fixed total electron number  $N_e$  and spin projection  $S_z$ . The space is spanned by the orthonormal Fock basis  $\mathcal{B} = \{|\mathbf{x}\rangle\}$ , where each basis vector is identified by an occupation bitstring  $\mathbf{x} \in \{0, 1\}^{N_o}$ . To avoid ambiguity with the determinant structure of the ansatz described in section 2.2, we refer to the basis elements  $|\mathbf{x}\rangle$  strictly as *configurations*. The many-body variational wavefunction is parameterized as a linear expansion  $|\Psi_\theta\rangle = \sum_{\mathbf{x} \in \mathcal{B}} \psi_\theta(\mathbf{x}) |\mathbf{x}\rangle$ , where  $\psi_\theta(\mathbf{x})$  denotes the real-valued amplitude computed by the neural network with trainable parameters  $\theta$ .

The optimization proceeds iteratively. At each outer iteration  $k$ , the wavefunction is supported on a variational set  $\mathcal{V}_k \subset \mathcal{B}$ . We define the connected set  $\mathcal{C}_k$  as the subset of all configurations coupled to  $\mathcal{V}_k$  via the Hamiltonian  $\hat{H}$ :

$$\mathcal{C}_k = |\mathbf{x}'\rangle \in \mathcal{B} \mid \exists |\mathbf{x}\rangle \in \mathcal{V}_k, \langle \mathbf{x}' | \hat{H} | \mathbf{x} \rangle \neq 0. \quad (1)$$

The external configurations are isolated in the perturbative set  $\mathcal{P}_k = \mathcal{C}_k \setminus \mathcal{V}_k$ . The union  $\mathcal{T}_k = \mathcal{V}_k \cup \mathcal{P}_k$  forms the target set for deterministic evaluation.

During the inner optimization loop,  $\mathcal{T}_k$  remains fixed. The parameters  $\theta$  are updated to minimize an energy objective defined over this target set. Upon convergence, a scoring function  $w(\mathbf{x}) = |\psi_\theta(\mathbf{x})|$  is evaluated for all  $|\mathbf{x}\rangle \in \mathcal{T}_k$  to select the updated variational set  $\mathcal{V}_{k+1}$  for the subsequent iteration. Table 1 summarizes the notation used throughout this work.

Table 1: Nomenclature and symbols used in this work.

Symbol	Description
<i>System and Wavefunction</i>	
$N_o, N_e$	Number of spin-orbitals and electrons.
$\mathbf{x} \in \{0, 1\}^{N_o}$	Occupation bitstring representing a configuration.
$ \mathbf{x}\rangle$	Orthonormal Fock basis vector.
$\theta$	Trainable parameters of the ansatz.
$\psi_\theta(\mathbf{x})$	Amplitude mapping $\mathbf{x} \mapsto \mathbb{R}$ .
$ \Psi_\theta\rangle$	Global variational wavefunction.
<i>Subset</i>	
$\mathcal{V}_k$	Variational set at iteration $k$ .
$\mathcal{C}_k$	Connected set coupled to $\mathcal{V}_k$ .
$\mathcal{P}_k$	Perturbative set, defined as $\mathcal{C}_k \setminus \mathcal{V}_k$ .
$\mathcal{T}_k$	Target set for deterministic evaluation, $\mathcal{V}_k \cup \mathcal{P}_k$ .
<i>Hamiltonians and Objectives</i>	
$\mathbf{H}_{\mathcal{X}\mathcal{Y}}$	Hamiltonian matrix block with rows in $\mathcal{X}$ and columns in $\mathcal{Y}$ .
$\tilde{\mathbf{H}}_k$	Proxy Hamiltonian defined on $\mathcal{T}_k$ .
$E_{\text{var/asym/proxy}}$	Variational, Asymmetric, and Proxy energy objectives.
$\Delta E_{\text{PT2}}$	Second-order perturbative correction.

## 2.2 Neural Network Quantum States

We parameterize the wavefunction amplitude  $\psi_\theta(\mathbf{x})$  using a NQS. A defining characteristic of NQS in fermionic systems is the enforcement of antisymmetry. Current architectures can be categorized into three classes based on their treatment of the sign structure:

1. **Unconstrained Architectures:** General-purpose function approximators, such as RBMs or MLPs, map configurations directly to amplitudes,  $\psi_\theta(\mathbf{x}) \approx \text{NN}(\mathbf{x})$ [14, 21, 23, 25]. Lacking an intrinsic antisymmetry mechanism, these models typically require complex-valued outputs or separate amplitude-phase networks to learn the sign structure. The resulting optimization landscape is highly non-convex, often necessitating pre-training or geometry-aware optimizers like Stochastic Reconfiguration[30–32].
2. **Slater-Jastrow Architectures:** These ansätze decompose the amplitude into a multiplicative Jastrow factor  $J_\theta(\mathbf{x})$  and a fixed reference determinant:  $\psi_\theta(\mathbf{x}) = e^{J_\theta(\mathbf{x})} \det(\mathbf{\Phi}_{\text{HF}}[\mathbf{x}])$ . While this strictly

enforces the sign structure of the reference state (e.g., Hartree–Fock), the fixed nodal surface limits accuracy in strongly correlated regimes where the ground-state sign structure deviates from the mean-field reference[33, 34].

**3. Neural Network Backflow Architectures:** Backflow transformations generalize the Slater determinant by making the single-particle orbitals dependent on the many-body configuration  $\mathbf{x}$ . By learning a configuration-dependent orbital basis  $\tilde{\phi}_i(\mathbf{x})$ , these architectures allow continuous deformation of the sign structure while preserving the determinant antisymmetry[22, 35].

In this work, we employ a single-determinant neural network backflow ansatz. Assuming a time-reversal symmetric Hamiltonian, the ground-state wavefunction can be taken as real-valued; thus, we utilize a real-valued neural network.

The ansatz is constructed from a static reference orbital matrix  $\Phi^0 \in \mathbb{R}^{N_o \times N_e}$ , obtained from Restricted Hartree–Fock (RHF). The backflow transformation introduces configuration dependence via a neural network  $\Delta\Phi_\theta : \{0, 1\}^{N_o} \rightarrow \mathbb{R}^{N_o \times N_e}$ . The effective orbital matrix  $\Phi_\theta(\mathbf{x})$  is defined as:

$$\Phi_\theta(\mathbf{x}) = \Phi^0 + \Delta\Phi_\theta(\mathbf{x}), \quad (2)$$

where  $\Delta\Phi_\theta(\mathbf{x})$  is a non-linear additive correction. This formulation incorporates many-body correlations directly into the single-particle basis.

For a configuration  $\mathbf{x}$ , let  $\mathcal{I}(\mathbf{x}) = \{i \mid x_i = 1\}$  denote the set of occupied orbital indices. The occupied submatrix  $\mathbf{A}_\theta(\mathbf{x}) \in \mathbb{R}^{N_e \times N_e}$  is constructed by selecting the rows of  $\Phi_\theta(\mathbf{x})$  indexed by  $\mathcal{I}(\mathbf{x})$ :

$$[\mathbf{A}_\theta(\mathbf{x})]_{jk} = [\Phi_\theta(\mathbf{x})]_{i_j, k}, \quad \text{where } i_j \in \mathcal{I}(\mathbf{x}). \quad (3)$$

The wavefunction amplitude is the determinant of this submatrix:

$$\psi_\theta(\mathbf{x}) = \det(\mathbf{A}_\theta(\mathbf{x})). \quad (4)$$

By implementing the network as a residual mapping and initializing weights such that  $\Delta\Phi_\theta(\mathbf{x}) \approx \mathbf{0}$ , the ansatz reduces to the Hartree–Fock state  $|\Phi_{\text{HF}}\rangle$  at the start of optimization. This ensures the optimization trajectory begins from a physically valid sign structure.

## 2.3 Deterministic Energy Objectives

We formulate the optimization problem by replacing stochastic expectation values with deterministic summations. The energy objective is defined as a functional  $E(\theta; \Omega, \hat{H}_{\text{eff}})$ , specified by a normalization domain  $\Omega$  and an effective Hamiltonian  $\hat{H}_{\text{eff}}$ . The general form is given by the Rayleigh quotient:

$$E(\theta; \Omega, \hat{H}_{\text{eff}}) = \frac{\langle \Psi_{\Omega} | \hat{H}_{\text{eff}} | \Psi_{\mathcal{T}} \rangle}{\langle \Psi_{\Omega} | \Psi_{\Omega} \rangle} = \frac{\sum_{\mathbf{x} \in \Omega} \psi_{\theta}(\mathbf{x}) \langle \mathbf{x} | \hat{H}_{\text{eff}} | \Psi_{\mathcal{T}} \rangle}{\sum_{\mathbf{x} \in \Omega} |\psi_{\theta}(\mathbf{x})|^2}, \quad (5)$$

where  $\Psi_{\mathcal{T}}$  denotes the wavefunction restricted to the target set  $\mathcal{T}_k$ . We analyze three distinct optimization modes derived from this functional.

### 2.3.1 Asymmetric Mode

This mode corresponds to deterministic schemes used in recent non-stochastic or semi-stochastic approaches [21, 22, 36]. The normalization is restricted to the variational set ( $\Omega = \mathcal{V}_k$ ), while the Hamiltonian expectation value includes contributions from the full target set ( $\hat{H}_{\text{eff}} = \hat{P}_{\mathcal{T}} \hat{H} \hat{P}_{\mathcal{T}}$ ). The energy is computed as the expectation value of the local energy  $E_{\text{loc}}(\mathbf{x})$ :

$$E_{\text{asym}}(\theta) = \sum_{\mathbf{x} \in \mathcal{V}_k} p_{\mathcal{V}}(\mathbf{x}) E_{\text{loc}}(\mathbf{x}), \quad E_{\text{loc}}(\mathbf{x}) = \sum_{\mathbf{x}' \in \mathcal{T}_k} H_{\mathbf{x}\mathbf{x}'} \frac{\psi_{\theta}(\mathbf{x}')}{\psi_{\theta}(\mathbf{x})}, \quad (6)$$

with  $p_{\mathcal{V}}(\mathbf{x}) = |\psi_{\theta}(\mathbf{x})|^2 / \sum_{\mathbf{y} \in \mathcal{V}_k} |\psi_{\theta}(\mathbf{y})|^2$ . A gradient estimator analogous to the VMC log-derivative trick is typically employed:

$$\mathbf{g}_{\text{asym}} = 2 \sum_{\mathbf{x} \in \mathcal{V}_k} p_{\mathcal{V}}(\mathbf{x}) (E_{\text{loc}}(\mathbf{x}) - E_{\text{asym}}) \nabla_{\theta} \ln |\psi_{\theta}(\mathbf{x})|. \quad (7)$$

Note that  $\mathbf{g}_{\text{asym}}$  is not the exact gradient of  $E_{\text{asym}}(\theta)$ , as it neglects terms arising from the dependence of  $E_{\text{loc}}(\mathbf{x})$  on the parameters via amplitudes in  $\mathcal{P}_k$ . Consequently, the resulting vector field is non-conservative. The derivation of the exact full gradient is provided in the Supporting Information.

### 2.3.2 Proxy Mode

The Proxy mode restores consistency between the energy functional and its gradient by extending the normalization domain to the full target set ( $\Omega = \mathcal{T}_k$ ) and employing a sparse effective Hamiltonian  $\tilde{\mathbf{H}}_k$ . The Proxy Hamiltonian  $\tilde{\mathbf{H}}_k$  retains exact off-diagonal elements involving  $\mathcal{V}_k$  but approximates the  $\mathcal{P}_k$ - $\mathcal{P}_k$  block diagonally:

$$(\tilde{\mathbf{H}}_k)_{\mathbf{x}\mathbf{y}} = \begin{cases} H_{\mathbf{x}\mathbf{y}} & \text{if } \mathbf{x} \in \mathcal{V}_k \text{ or } \mathbf{y} \in \mathcal{V}_k, \\ H_{\mathbf{x}\mathbf{x}} \delta_{\mathbf{x}\mathbf{y}} & \text{if } \mathbf{x}, \mathbf{y} \in \mathcal{P}_k. \end{cases} \quad (8)$$

This approximation avoids the  $O(|\mathcal{P}|^2)$  cost of evaluating the full Hamiltonian on the perturbative set. The objective function is the exact Rayleigh quotient of  $\tilde{\mathbf{H}}_k$ :

$$E_{\text{proxy}}(\theta) = \frac{\langle \Psi_{\mathcal{T}} | \tilde{\mathbf{H}}_k | \Psi_{\mathcal{T}} \rangle}{\langle \Psi_{\mathcal{T}} | \Psi_{\mathcal{T}} \rangle}. \quad (9)$$

Since  $\tilde{\mathbf{H}}_k$  is Hermitian and  $\Omega$  matches the operator's domain, the gradient is well-defined:

$$\nabla_{\theta} E_{\text{proxy}} = \frac{2}{\langle \Psi_{\mathcal{T}} | \Psi_{\mathcal{T}} \rangle} \sum_{\mathbf{x} \in \mathcal{T}_k} \left[ \sum_{\mathbf{x}' \in \mathcal{T}_k} (\tilde{\mathbf{H}}_k)_{\mathbf{x}\mathbf{x}'} \psi_{\theta}(\mathbf{x}') - E_{\text{proxy}} \psi_{\theta}(\mathbf{x}) \right] \nabla_{\theta} \psi_{\theta}(\mathbf{x}). \quad (10)$$

This formulation provides explicit feedback from amplitudes in  $\mathcal{P}_k$ , stabilizing optimization in systems with strong coupling to the perturbative set.

### 2.3.3 Variational Mode

The Variational mode restricts the optimization to the variational subspace  $\mathcal{V}_k$  ( $\Omega = \mathcal{V}_k$ ), with the effective Hamiltonian defined as the projection  $\hat{H}_{\text{eff}} = \hat{P}_{\mathcal{V}} \hat{H} \hat{P}_{\mathcal{V}}$ . The objective is the standard variational energy within  $\mathcal{V}_k$ :

$$E_{\text{var}}(\theta) = \frac{\langle \Psi_{\mathcal{V}} | \hat{H} | \Psi_{\mathcal{V}} \rangle}{\langle \Psi_{\mathcal{V}} | \Psi_{\mathcal{V}} \rangle}. \quad (11)$$

The gradient corresponds to the projection of the residual vector onto the ansatz tangent space within  $\mathcal{V}_k$ :

$$\nabla_{\theta} E_{\text{var}} = \frac{2}{\langle \Psi_{\mathcal{V}} | \Psi_{\mathcal{V}} \rangle} \sum_{\mathbf{x} \in \mathcal{V}_k} \left[ \sum_{\mathbf{x}' \in \mathcal{V}_k} H_{\mathbf{x}\mathbf{x}'} \psi_{\theta}(\mathbf{x}') - E_{\text{var}} \psi_{\theta}(\mathbf{x}) \right] \nabla_{\theta} \psi_{\theta}(\mathbf{x}). \quad (12)$$

This mode learns a non-linear compression of the ground state wavefunction within  $\mathcal{V}_k$ . Since contributions from  $\mathcal{P}_k$  are neglected during optimization, this approach is designed to be coupled with post-optimization perturbative corrections (e.g., PT2) to recover dynamic correlation.

## 2.4 Self-Consistent Optimization and Subspace Evolution

We adopt a self-consistent optimization procedure that interleaves parameter updates with adaptive refinement of the configuration set. This approach decomposes the problem into two alternating steps: minimizing the energy with respect to the ansatz parameters and discretely updating the wavefunction support. The algorithm creates a feedback loop between the effective Hamiltonian, projected onto the current variational subspace, and the neural wavefunction, whose amplitudes determine the set for the subsequent iteration.

#### 2.4.1 Inner Loop: Parameter Optimization

In the inner loop, the target set  $\mathcal{T}_k$  and the corresponding effective Hamiltonian (e.g.,  $\tilde{\mathbf{H}}_k$  or  $\hat{P}_{\mathcal{V}}\hat{H}\hat{P}_{\mathcal{V}}$ ) are fixed. The objective is to minimize the deterministic energy functional  $E(\theta; \mathcal{T}_k)$  with respect to  $\theta$ .

Unlike stochastic VMC, the energy and gradients are computed via exact summation over  $\mathcal{T}_k$ , resulting in a deterministic optimization landscape without sampling noise. Since the effective Hamiltonian and the support  $\mathcal{T}_k$  evolve across outer iterations, the network optimizes against a dynamic dataset. This requires the ansatz to learn generalized correlation rules to estimate amplitudes for new configurations entering the set, effectively regularizing the network against overfitting to a static set of configurations.

#### 2.4.2 Outer Loop: Subspace Evolution

The outer loop updates the variational basis  $\mathcal{V}_k \rightarrow \mathcal{V}_{k+1}$  to capture the relevant sector of the Hilbert space. This step functions as a selection operator  $\mathcal{S} : \mathcal{T}_k \rightarrow \mathcal{V}_{k+1}$ , constructing the new variational set based on the amplitude distribution  $|\psi_{\theta}(\mathbf{x})|$  of the current wavefunction. This evolution relies on the neural network's ability to model wavefunction sparsity, assigning large amplitudes to significant configurations even if they currently reside in the perturbative set  $\mathcal{P}_k$ .

We consider three protocols for subspace selection:

1. **Fixed-Size (Top- $K$ ) Selection:** The variational set retains the  $N_v$  configurations with the largest amplitudes. This imposes an explicit upper bound on memory usage and computational cost, ensuring consistent performance on hardware resources [37].
2. **Cumulative Mass Selection:** The set expands to include the minimal set of configurations accounting for a target fraction  $\gamma \in (0, 1]$  of the total probability mass normalized over  $\mathcal{T}_k$ .
3. **Absolute Threshold Selection:** All configurations with a normalized probability  $p(\mathbf{x}) > \epsilon$  are retained. This criterion ensures a uniform resolution of the wavefunction but does not bound the subspace dimension [21, 38].

In this work, we primarily use the Top- $K$  protocol. This choice decouples the memory footprint from the Hilbert space dimension, providing control over the computational budget and GPU memory utilization.

#### 2.4.3 Post-Optimization Correction

Upon convergence, post-hoc evaluations refine the energy estimate. For the Proxy and Asymmetric modes, the bias from approximate Hamiltonians is removed by evaluating the exact Rayleigh quotient over the final

target set  $\mathcal{T} = \mathcal{V} \cup \mathcal{P}$ . Since the ansatz  $\Psi_\theta$  is defined globally, the variational energy can also be estimated via standard VMC sampling [37].

In the Variational mode, optimization is confined to  $\mathcal{V}$ . We recover correlations from the perturbative set using Epstein–Nesbet PT2. A key distinction from linear CI is that the optimized NQS is not an exact eigenstate of the projected Hamiltonian  $\hat{P}_\mathcal{V} \hat{H} \hat{P}_\mathcal{V}$ . Therefore, the perturbative correction must account for the non-vanishing residual within  $\mathcal{V}$  alongside the coupling to  $\mathcal{P}$  [38, 39]. The total corrected energy is  $E_{\text{tot}} = E_{\text{var}} + \Delta E_{\text{PT2}}$ , with:

$$\Delta E_{\text{PT2}} = \sum_{\mathbf{x} \in \mathcal{V}} \frac{|\langle \mathbf{x} | \hat{H} - E_{\text{var}} | \Psi_{\mathcal{V}} \rangle|^2}{E_{\text{var}} - H_{\mathbf{xx}}} + \sum_{\mathbf{x} \in \mathcal{P}} \frac{|\langle \mathbf{x} | \hat{H} | \Psi_{\mathcal{V}} \rangle|^2}{E_{\text{var}} - H_{\mathbf{xx}}}. \quad (13)$$

The first term corrects for the internal approximation error of the ansatz within  $\mathcal{V}$ , while the second term captures the contribution from the perturbative set  $\mathcal{P}$ .

### 3 Computational Implementation and Acceleration

Implementing a deterministic NQS framework for large-scale molecular systems requires handling two distinct computational workloads: the combinatorial generation of sparse Hamiltonian graphs and the differentiable optimization of high-dimensional wavefunction ansätze. The former involves integer bitwise operations and irregular memory access patterns typical of sCI methods. The latter relies on heavy floating-point tensor contractions and automatic differentiation (AD) characteristic of deep learning workflows. To address these differing requirements, we implemented a three-tier hybrid architecture that separates discrete combinatorial logic from differentiable numerical computation, facilitating the integration of classical quantum chemistry algorithms with modern hardware accelerators.

#### 3.1 Hybrid Architecture

The software stack consists of three layers, assigning computational tasks to the backend best suited for their arithmetic intensity and data structure requirements:

1. **Layer 0 (L0) - C++ Combinatorial Kernel:** This kernel layer handles the discrete algebra of the Fock space. Implemented in C++ and exposed to Python via `nanobind`[40], L0 manages molecular integrals and precomputed heat-bath tables within a persistent `IntCtx` (Integral Context). Operating directly on 64-bit integer representations of configurations, it efficiently evaluates Slater–Condon rules, generates the configuration graph, and constructs Hamiltonian matrices ( $\mathbf{H}_{\mathcal{V}\mathcal{V}}$ ,  $\mathbf{H}_{\mathcal{V}\mathcal{P}}$ ) in Compressed

Sparse Row (CSR) format. Executing these branching-heavy operations in compiled C++ avoids the interpreter overhead associated with high-level languages.

2. **Layer 1 (L1) - Python Orchestration:** This intermediate layer manages the control flow of the self-consistent field cycle. It controls the "Outer Loop": invoking L0 to rebuild Hamiltonian blocks for the evolving subspace  $\mathcal{V}_k$ , maintaining global state variables, and applying screening criteria for subspace expansion. L1 acts as a data bridge, transferring only necessary topological data—sparse indices and matrix values—from the discrete kernel to the differentiable core.
3. **Layer 2 (L2) - JAX Differentiable Core:** Numerical optimization of the NQS parameters is performed within the "Inner Loop", implemented entirely in JAX[41]. We use the XLA (Accelerated Linear Algebra) compiler to Just-In-Time (JIT) compile wavefunction inference, energy accumulation, and gradient backpropagation into a single fused computation graph. This end-to-end compilation allows the optimization step to execute on the GPU without returning control to the host, eliminating Python interpreter overhead and maximizing memory bandwidth. For the H<sub>2</sub>O (6-31G) system ( $|\mathcal{V}| = 8192$ ), JIT compilation reduces the per-step execution time by a factor of  $\sim 33$  (from 234 ms to 7 ms).

### 3.2 Memory Management and Host-Resident Operations

Deterministic summation over target sets depends explicitly on the subspace size  $|\mathcal{T}_k|$ , creating memory requirements distinct from stochastic sampling. Two primary constraints arise: the storage for the sparse Hamiltonian matrix, which grows linearly with the number of non-zero elements, and the VRAM footprint for neural network gradient computation, which scales with batch size. To manage these constraints, we use a heterogeneous memory strategy utilizing both host and device resources.

**Host-Resident Sparse Matrix-Vector Product (SpMV):** For large systems, the sparse Hamiltonian  $\mathbf{H}_{\mathcal{T}\mathcal{T}}$  often exceeds GPU memory capacity. We adopt a host-resident strategy where the Hamiltonian is stored exclusively in system RAM using the Compressed Sparse Row (CSR) format. During the inner optimization loop, the matrix-vector product  $\mathbf{v} = \mathbf{H}\psi$  executes on the CPU. We use the `jax.pure_callback` mechanism to invoke optimized SciPy[42] sparse routines within the JIT-compiled function. This offloads the irregular memory access of sparse algebra to the CPU and decouples the maximum treatable set size from GPU memory limits. While this introduces latency due to Host-Device data transfer over PCIe, this cost is generally masked by the compute-intensive neural network operations on the GPU.

**Scan-based Chunking for Gradient Accumulation:** Calculating the vector-Jacobian product (VJP) for the ansatz  $\psi_\theta(\mathbf{x})$  requires storing intermediate activation tensors. For target sets with millions of configurations, a single forward-backward pass exceeds available VRAM. We implement a chunking scheme using

the `jax.lax.scan` primitive. The target batch  $\mathcal{T}_k$  is partitioned into fixed-size blocks (e.g., 8192 configurations), with evaluation and gradient accumulation performed sequentially over these blocks within a single compiled kernel. Peak VRAM usage is thus determined by the chunk size and network architecture rather than the total subspace size  $|\mathcal{T}_k|$ , allowing the framework to process target sets larger than device memory, limited only by computation wall-time.

### 3.3 Acceleration via Heat-Bath Screening

The size of the connected subset  $\mathcal{C}_k$  scales as  $O(N_e^2 N_o^2)$  relative to the variational set  $\mathcal{V}_k$ . While enumerating these connections uses fast integer logic, the primary bottleneck is evaluating the neural network ansatz over the resulting target set  $\mathcal{T}_k = \mathcal{V}_k \cup \mathcal{P}_k$ . For both gradient accumulation (Proxy/Asymmetric modes) and subspace evolution (Variational mode), neural network inference and amplitude sorting over an unpruned  $\mathcal{T}_k$  can exceed GPU memory limits as the active space grows. To address this, we apply a deterministic screening strategy adapted from the Heat-Bath Configuration Interaction (HCI) algorithm[5, 43] to bound the size of the perturbative set  $\mathcal{P}_k$ .

The screening criterion filters configurations based on first-order perturbative coupling. A candidate configuration  $|\mathbf{x}'\rangle$  is included in the target set  $\mathcal{T}_k$  only if the Hamiltonian matrix element connecting it to the variational set satisfies:

$$\max_{|\mathbf{x}\rangle \in \mathcal{V}_k} |H_{\mathbf{x}'\mathbf{x}} \psi_\theta(\mathbf{x})| \geq \epsilon_{\text{HB}}, \quad (14)$$

where  $\psi_\theta(\mathbf{x})$  is the amplitude of the reference state and  $\epsilon_{\text{HB}}$  is a numerical threshold.

Applying Eq. 14 directly requires iterating over all double excitations. To avoid this  $O(N^4)$  cost, we utilize the structure of two-electron integrals. During initialization, we precompute a lookup table where, for each pair of occupied spin-orbitals  $(i, j)$ , corresponding pairs of virtual orbitals  $(a, b)$  are sorted in descending order of integral magnitude  $|\langle ij || ab \rangle|$ .

During subspace expansion, this sorted structure enables an efficient “early exit” generation algorithm. For a given configuration  $|\mathbf{x}\rangle$  with amplitude  $\psi_\theta(\mathbf{x})$ , we define a dynamic cutoff  $\tau = \epsilon_{\text{HB}}/|\psi_\theta(\mathbf{x})|$ . The algorithm iterates through the pre-sorted virtual pairs for each occupied pair in  $|\mathbf{x}\rangle$ , terminating the loop when  $|\langle ij || ab \rangle| < \tau$ . Configurations with negligible coupling are thus never generated. This shifts the computational complexity of the expansion step from scaling with the total number of orbitals to scaling with the number of significant Hamiltonian entries. By controlling the size of  $\mathcal{T}_k$ , screening ensures that the memory footprint of the sparse Hamiltonian and the batch size for neural network inference remain tractable.

### 3.4 Overview and Optimization Details

Algorithm 1 summarizes the deterministic optimization workflow. Unless noted otherwise, benchmark parameters are as follows. Molecular Hamiltonians are constructed using one- and two-body integrals from Restricted Hartree–Fock (RHF) calculations via the PySCF package [44–46]. The variational set  $\mathcal{V}_0$  is initialized with the single Hartree–Fock configuration.

We use a Multi-Layer Perceptron (MLP) with two hidden layers of 256 units (Input-256-256-Output) to parameterize the backflow correction  $\Delta\Phi_\theta$ . Parameters are initialized randomly without pre-training. Computations use double precision (fp64) in JAX with Just-In-Time (JIT) compilation. The heat-bath screening threshold for the perturbative set is  $\epsilon_{\text{HB}} = 10^{-6}$ .

Optimization uses the AdamW algorithm with weight decay. The learning rate follows a cosine decay schedule, decreasing from  $10^{-3}$  to  $5 \times 10^{-5}$  over 800 steps. Calculations involve  $N_{\text{outer}} = 30$  outer iterations for subspace evolution. In each outer iteration, we perform  $N_{\text{inner}} = 1000$  gradient descent steps to optimize ansatz parameters on the fixed set. Large target set evaluations use a chunk size of 8192 to manage GPU memory. Benchmarks were run on a single NVIDIA A100 (80GB) GPU with 8 Intel Xeon Gold 8358 CPU cores and 128GB RAM.

## 4 Results and Discussions

We present numerical results to validate the accuracy and efficiency of the deterministic framework. The analysis begins with an evaluation of the optimization modes and convergence properties on the water molecule. We then benchmark ground-state energies for small molecules against FCI and stochastic NQS methods, followed by an investigation of bond dissociation curves for  $\text{H}_2\text{O}$  and  $\text{N}_2$ . Finally, we apply the framework to the strongly correlated chromium dimer ( $\text{Cr}_2$ ) and analyze the wall-time scaling of the hybrid implementation.

### 4.1 Performance of Deterministic Optimization Modes

We first evaluate the convergence characteristics of the Variational, Asymmetric, and Proxy modes using  $\text{H}_2\text{O}$  in the 6-31G basis set. Figure 1 displays the energy error relative to the FCI limit as a function of wall time and variational set size  $|\mathcal{V}|$ .

The wall-time trajectories in Figure 1(a) distinguish the computational costs of the three approaches. The Variational mode achieves the lowest cost per iteration because wavefunction evaluation and gradient backpropagation are strictly confined to the variational set  $\mathcal{V}$ , avoiding the computationally expensive

---

**Algorithm 1** Deterministic Optimization of Neural Network Quantum States (Variational Mode)

---

1: **Input:** Hamiltonian integrals (FCIDUMP), Ansatz  $\Psi_\theta$ , Hyperparameters ( $N_{\text{outer}}$ ,  $N_{\text{inner}}$ ,  $\epsilon_{\text{HB}}$ ,  $K$ )  
2: **Output:** Optimized parameters  $\theta^*$ , Final Energy  $E_{\text{total}}$

3: Initialize parameters  $\theta$  and variational set  $\mathcal{V}_0 \leftarrow \{|\Phi_{\text{HF}}\rangle\}$   
4: **for**  $k = 1$  to  $N_{\text{outer}}$  **do** ▷ Outer Loop: Subspace Evolution

5:   **1. Deterministic Subspace Expansion (Layer 0)**  
6:     Transfer amplitudes  $\psi_\theta(\mathcal{V}_{k-1})$  to host  
7:     Generate screened perturbative set  $\mathcal{P}_k$  via heat-bath criteria:  
8:      $\mathcal{P}_k \leftarrow \{|\mathbf{x}'\rangle \notin \mathcal{V}_{k-1} \mid \max_{\mathbf{x} \in \mathcal{V}_{k-1}} |H_{\mathbf{x}'\mathbf{x}}\psi_\theta(\mathbf{x})| \geq \epsilon_{\text{HB}}\}$  ▷ [CPU] C++ Kernel  
9:     Construct sparse Hamiltonian block  $\mathbf{H}_{\mathcal{V}\mathcal{V}}$  ▷ [CPU] nanobind

10:   **2. Differentiable Parameter Optimization (Layer 2)**  
11:     Transfer active configurations  $\mathcal{V}_{k-1}$  to device memory  
12:     **JIT Compile** optimization step (fused forward/backward pass):  
13:     **for**  $t = 1$  to  $N_{\text{inner}}$  **do** ▷ Inner Loop  
14:       Compute amplitudes  $\psi_\theta(\mathcal{V}_{k-1})$  via chunked inference ▷ [GPU] lax.scan  
15:       Compute matrix-vector product  $\mathbf{v} = \mathbf{H}_{\mathcal{V}\mathcal{V}}\psi$  ▷ [CPU] pure\_callback  
16:        $\mathcal{L}(\theta) \leftarrow E_{\text{var}} = \frac{\langle \Psi_{\mathcal{V}} | \hat{H} | \Psi_{\mathcal{V}} \rangle}{\langle \Psi_{\mathcal{V}} | \Psi_{\mathcal{V}} \rangle}$   
17:       Compute gradients  $\nabla_\theta \mathcal{L}$  via AD  
18:       Update  $\theta \leftarrow \text{Optimizer}(\theta, \nabla_\theta \mathcal{L})$  ▷ [GPU] Update  
19:     **end for**

20:   **3. Subspace Pruning (Layer 1)**  
21:     Evaluate wavefunction amplitudes on full target set  $\mathcal{T}_k$   
22:      $\mathcal{V}_k \leftarrow \text{Selector}(\mathcal{T}_k, K, \text{key} = |\psi_\theta|)$  ▷ [CPU] Sorting  
23:     **end for**

24: **4. Post-Optimization Correction**  
25: Compute  $E_{\text{var}}$  on final set  $\mathcal{V}_{N_{\text{outer}}}$   
26: Compute perturbative correction  $\Delta E_{\text{PT2}}$   
27: **return**  $\theta^*, E_{\text{total}} = E_{\text{var}} + \Delta E_{\text{PT2}}$

---

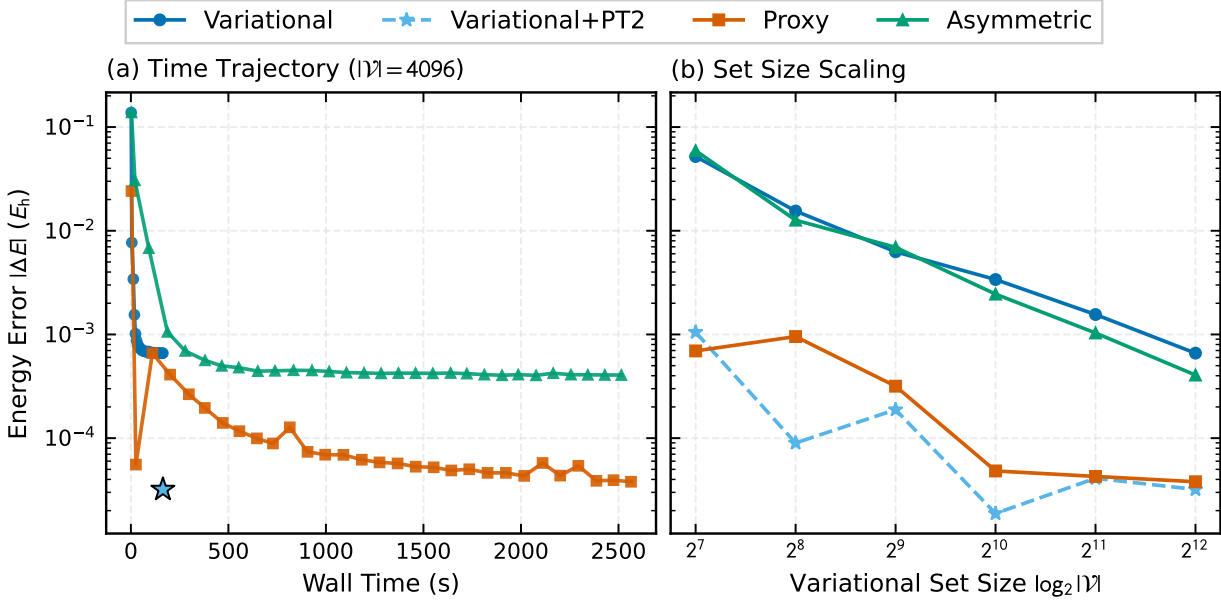


Figure 1: Convergence of deterministic objectives for H<sub>2</sub>O (6-31G). (a) Energy error  $|\Delta E|$  relative to FCI versus wall time for a fixed variational set  $|\mathcal{V}| = 4096$ . (b) Final energy error versus variational set size  $\log_2 |\mathcal{V}|$ .

enumeration of the connected set  $\mathcal{C}$ . While the pure Variational energy is bounded by the representational capacity of  $\mathcal{V}$  (solid blue line), the addition of the second-order Epstein-Nesbet perturbation correction (Variational+PT2, dashed blue line) recovers the majority of the missing dynamic correlation without increasing the optimization cost.

Regarding the target-space formulations ( $\mathcal{T} = \mathcal{V} \cup \mathcal{P}$ ), the Proxy mode (orange line) yields significantly lower errors than the Asymmetric mode (green line). The stagnation of the Asymmetric mode near the uncorrected Variational result indicates that evaluating Hamiltonian connections into  $\mathcal{P}$  is ineffective without a consistent gradient signal. The gradient estimator in the Asymmetric mode neglects the parameter dependence of amplitudes in the perturbative set ( $\nabla_\theta \psi(\mathbf{x})$  for  $\mathbf{x} \in \mathcal{P}$ ), resulting in a non-conservative vector field. In contrast, the Proxy mode minimizes the exact Rayleigh quotient of a Hermitian effective Hamiltonian  $\tilde{\mathbf{H}}$  defined on  $\mathcal{T}$ . This ensures mathematical consistency between the energy functional and its gradient, allowing the optimization to effectively incorporate contributions from the perturbative set.

The error scaling with respect to subspace size  $|\mathcal{V}|$  (Figure 1(b)) demonstrates that the Proxy mode and the Variational+PT2 strategy yield comparable accuracy. This agreement suggests that the post-optimization perturbative correction effectively captures the same dynamic correlations from  $\mathcal{P}$  that are treated self-consistently in the Proxy formulation. However, the Proxy mode requires evaluating gradients over the full target set  $\mathcal{T}$  at every step, whereas the PT2 correction is a non-iterative calculation performed

only upon convergence. Given its superior computational efficiency, we adopt the Variational+PT2 protocol as the standard approach for the subsequent benchmarks.

## 4.2 Benchmarks on Molecular Systems

We evaluate the scalability and accuracy of the deterministic framework by computing the ground-state energies of  $\text{Li}_2\text{O}$ ,  $\text{C}_2\text{H}_4\text{O}$ , and  $\text{C}_3\text{H}_8$ . These systems encompass Hilbert spaces ranging from  $10^7$  to  $10^{12}$  configurations. Table 2 summarizes the calculated energies alongside results from FCI, CCSD(T), and existing NQS benchmarks.

A key difference between this work and previous deterministic or semi-deterministic NQS approaches (e.g., SC-RBM [21, 38], NNBF [22, 37]) lies in the optimization domain. Previous methods typically incorporate the connected set  $\mathcal{C}$  or a target set  $\mathcal{T}$  into the gradient estimator to capture dynamic correlation during training. This strategy incurs a computational cost scaling of  $O(N_e^2 N_o^2 |\mathcal{V}|)$  and involves non-conservative gradient fields. In contrast, the present Variational Mode restricts both wavefunction evaluation and gradient backpropagation strictly to the variational set  $\mathcal{V}$ . This reduces the optimization complexity to  $O(|\mathcal{V}|)$  and ensures a rigorous Hermitian minimization of the projected Hamiltonian  $P_{\mathcal{V}} \hat{H} P_{\mathcal{V}}$ . This approach effectively decouples the problem: the neural ansatz optimizes the static correlation within a compact  $\mathcal{V}$ , while the residual dynamic correlation is recovered via the post-hoc PT2 correction.

For  $\text{Li}_2\text{O}$ , strictly variational minimization within a compact set proves efficient. Using  $|\mathcal{V}| = 2048$ , the variational energy ( $-87.891\,996$  Ha) is lower than the SC-RBM result obtained with a similar approach ( $-87.891\,8$  Ha) [21]. This indicates that optimizing the ansatz within a closed, mathematically consistent manifold yields a lower energy bound compared to trajectories influenced by approximate gradients from the perturbative set. As  $|\mathcal{V}|$  expands to 131 072, the total energy (Variational+PT2) converges to the FCI limit within micro-Hartree accuracy.

For  $\text{C}_2\text{H}_4\text{O}$ , where the Hilbert space exceeds  $10^9$ , we compare our results against the autoregressive MADE[47] and NAQS[25] architecture. Our variational energy using 2048 configurations ( $-151.104\,900$  Ha) is lower than the MADE benchmark ( $-151.092\,983$  Ha). While autoregressive models rely on unbiased sampling, the deterministic Top- $K$  selection imposes a strong inductive bias that prioritizes configurations based on amplitude magnitude. This allows the ansatz to identify dominant configurations in highly sparse wavefunctions without the variance associated with stochastic sampling.

The  $\text{C}_3\text{H}_8$  molecule represents a regime ( $10^{12}$  configurations) where exact enumeration is intractable. Comparison with recent distributed FCI benchmarks [48] shows systematic convergence. Expanding  $|\mathcal{V}|$  from 131 072 to 524 288 reduces the total energy error relative to FCI from 0.96 mHa to 0.47 mHa. The

results demonstrate that while the variational optimization captures the multi-configuration nature of the reference state, the perturbative correction is essential for recovering the remaining dynamic correlation energy in large basis sets.

### 4.3 Dissociation of $\text{H}_2\text{O}$ and $\text{N}_2$

We computed potential energy surfaces (PES) for the symmetric dissociation of  $\text{H}_2\text{O}$  and the bond breaking of  $\text{N}_2$  using the cc-pVDZ basis set. Reference ground-state energies were obtained from FCI data by Olsen et al.[49] for  $\text{H}_2\text{O}$ , and DMRG ( $M = 4000$ )[50] and CDFCI[51] benchmarks for  $\text{N}_2$ .

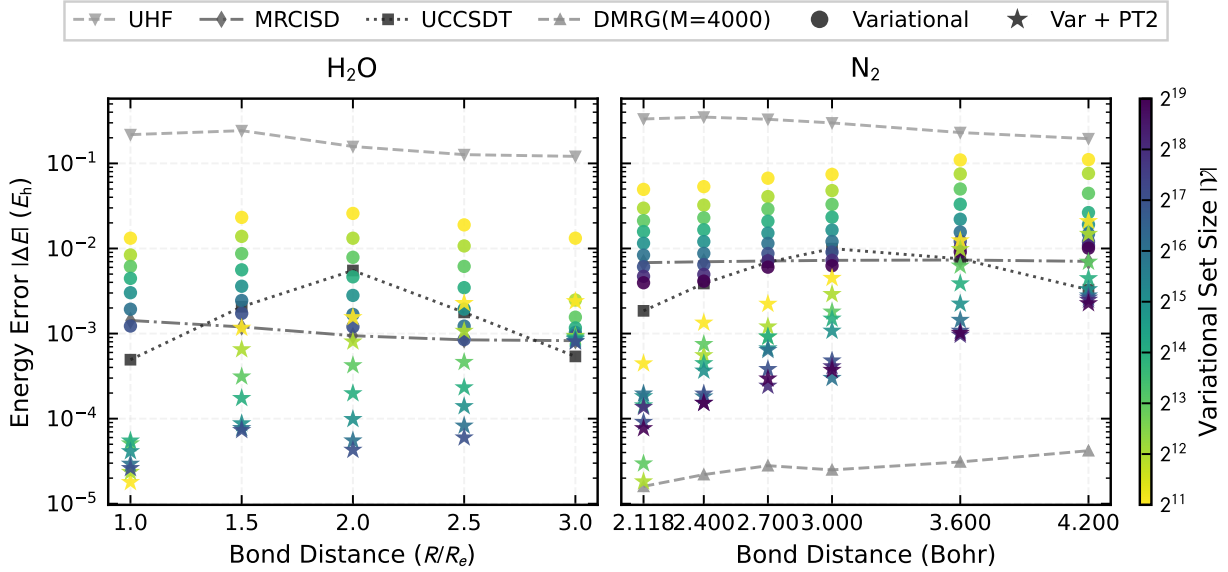


Figure 2: Absolute energy errors  $|\Delta E|$  relative to FCI/CDFCI benchmarks for the symmetric dissociation of  $\text{H}_2\text{O}$  (left) and  $\text{N}_2$  (right) in the cc-pVDZ basis set. Results are shown for the Variational mode (circles) and the Variational+PT2 scheme (stars). The color gradient indicates the size of the variational set  $|\mathcal{V}|$ , ranging from  $2^{13}$  (yellow) to  $2^{17}$  (dark purple). Baselines including UHF, MRCISD, UCCSDT, and DMRG are plotted for comparison.

Figure 2 presents the absolute energy errors relative to the benchmarks. For  $\text{H}_2\text{O}$  (left panel), the single-reference UCCSDT method diverges from the FCI limit as the O-H bonds stretch, with errors increasing by approximately two orders of magnitude at  $3.0R/R_e$ . This reflects the inadequacy of the single-configuration reference in the bond-breaking regime. The NNBF ansatz, optimized via the Variational mode and augmented with second-order perturbation theory (Variational+PT2), maintains consistent accuracy across the dissociation coordinate. With a variational set of  $|\mathcal{V}| = 2^{17}$ , the Variational+PT2 energies remain within  $10^{-4}$  Ha of the FCI reference, yielding lower errors than both UCCSDT and MRCISD at large bond distances.

The dissociation of  $\text{N}_2$  (right panel) involves breaking a triple bond, introducing strong static correlation. The UCCSDT baseline exhibits a non-monotonic error distribution with a maximum deviation around 3.0

Table 2: Ground-state energies (in Hartree) calculated by our deterministic framework compared with previous NQS benchmarks and FCI/CCSD(T) references.  $|\mathcal{V}|$  denotes the size of the variational set. For our method, ‘Variational Energy’ refers to the exact expectation value  $E = \langle \Psi_{\mathcal{V}} | \hat{H} | \Psi_{\mathcal{V}} \rangle / \langle \Psi_{\mathcal{V}} | \Psi_{\mathcal{V}} \rangle$ , and ‘Total Energy’ includes the post-optimization PT2 correction. Methods are sorted by variational energy (descending) within each system.

Method	$ \mathcal{V} $	Variational Energy	Total Energy
<i>Li<sub>2</sub>O (STO-3G, 14e, 15o,  H  ≈ 4.14 × 10<sup>7</sup>)</i>			
FCI	-	-87.892 693	-
CCSD(T)	-	-	-87.893 089
MADE [47]	-	-87.885 637	-
<b>This work</b>	512	-87.887 889	-87.892 584
SC-RBM [21]	-	-87.8918	-
<b>This work</b>	2 048	-87.891 996	-87.892 680
NAQS [25]	-	-87.892 433	-
<b>This work</b>	8 192	-87.892 541	-87.892 689
Transformer [23]	-	-87.8926	-
<b>This work</b>	32 768	-87.892 646	-87.892 691
NNBF [22]	-	-87.892 662	-
<b>This work</b>	131 072	-87.892 662	-87.892 692
<i>C<sub>2</sub>H<sub>4</sub>O (STO-3G, 24e, 19o,  H  ≈ 2.54 × 10<sup>9</sup>)</i>			
FCI	-	-151.123 570	-
CCSD(T)	-	-	-151.122 748
<b>This work</b>	512	-151.047 686	-151.115 556
MADE [47]	-	-151.092 983	-
<b>This work</b>	2 048	-151.104 900	-151.121 939
<b>This work</b>	8 192	-151.114 672	-151.122 729
<b>This work</b>	32 768	-151.119 006	-151.123 226
NAQS [25]	-	-151.120 486	-
<b>This work</b>	131 072	-151.121 237	-151.123 361
<b>This work</b>	524 288	-151.122 393	-151.123 470
Transformer [23]	-	-151.1228	-
NNBF [22]	-	-151.123 357	-
<i>C<sub>3</sub>H<sub>8</sub> (STO-3G, 26e, 23o,  H  ≈ 1.31 × 10<sup>12</sup>)</i>			
FCI [48]	-	-117.100 123	-
CCSD(T)	-	-	-117.099 709
<b>This work</b>	512	-116.967 731	-117.088 963
<b>This work</b>	2 048	-117.068 360	-117.095 751
<b>This work</b>	8 192	-117.082 970	-117.097 458
<b>This work</b>	32 768	-117.087 785	-117.098 339
<b>This work</b>	131 072	-117.092 824	-117.099 158
<b>This work</b>	524 288	-117.096 772	-117.099 649

Bohr. This behavior arises from the symmetry-broken UHF reference, where spin contamination and the multireference character of the wavefunction compromise accuracy in the intermediate coupling regime.

As shown in Figure 2 (right), increasing  $|\mathcal{V}|$  from  $2^{13}$  to  $2^{17}$  systematically reduces the variational energy error. The inclusion of the PT2 correction recovers residual dynamic correlation, particularly near the equilibrium geometry where it reduces errors to below the MRCISD baseline. While the relative magnitude of the perturbative correction decreases at the dissociation limit—where static correlation dominates—the combined Variational+PT2 scheme remains accurate across all bond lengths. Chemical accuracy is obtained using a subspace of approximately  $10^5$  configurations. Given that the full Hilbert space for  $\text{N}_2$  exceeds  $10^{12}$ , this result indicates that the optimized backflow ansatz effectively encodes the sparsity of the wavefunction within a compact set.

#### 4.4 Chromium Dimer

The chromium dimer ( $\text{Cr}_2$ ) serves as a benchmark for balancing strong static and dynamic correlation. We computed the ground state energy at a bond length of 1.5 Å using the Ahlrichs SV basis set. To ensure comparability with Selected CI (HCI) [52], DMRG [53], and stochastic NQS methods (SC-RBM [38], Transformer [36]), all calculations utilize identical molecular orbitals derived from CASSCF(12e, 12o). Results for the CAS(24e, 30o) and CAS(48e, 42o) active spaces are summarized in Table 3 and Figure 3.

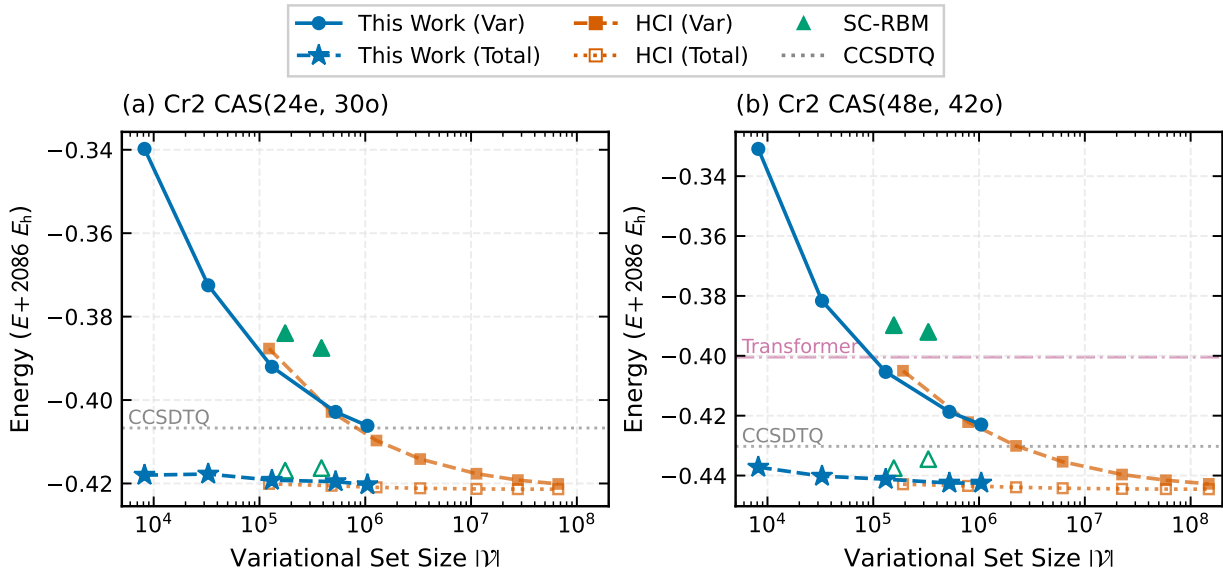


Figure 3: Convergence of variational (circles) and PT2-corrected total energies (stars) for  $\text{Cr}_2$  as a function of the variational set size  $|\mathcal{V}|$ . (a) CAS(24e, 30o) and (b) CAS(48e, 42o). Reference data include HCI (orange squares), SC-RBM (green triangles), Transformer (pink dashed line), and CCSDTQ (gray dotted line).

In the CAS(24e, 30o) system (System I, Hilbert space  $\sim 7.5 \times 10^{15}$ ), the deterministic framework achieves

lower variational energies with smaller subspace sizes compared to stochastic baselines. As shown in Figure 3(a), at  $|\mathcal{V}| = 8,192$ , the PT2-corrected total energy ( $-0.418002$  Ha) is lower than the CCSDTQ reference ( $-0.406696$  Ha), suggesting the recovery of correlation energy from high-order excitations. Comparing the variational energy at similar subspace sizes, our result at  $|\mathcal{V}| \approx 1.31 \times 10^5$  ( $-0.392029$  Ha) is approximately 8 mHa lower than the SC-RBM result ( $-0.38396$  Ha), which employs a support of  $\sim 1.75 \times 10^5$ . Upon expanding  $|\mathcal{V}|$  to  $10^6$ , the total energy converges to  $-0.420278$  Ha, consistent with DMRG and FCIQMC limits.

For the larger CAS(48e, 42o) active space (System II, Hilbert space  $> 10^{23}$ ), single-reference CCSDTQ overestimates the energy by  $\sim 14$  mHa relative to DMRG. Figure 3(b) shows that the deterministic ansatz yields variational energies lower than reported Transformer results. The final total energy of  $-0.442497$  Ha is within 2 mHa of the statistical limits established by HCI and DMRG ( $\approx -0.4445$  Ha).

The variational energy trajectory generally follows the HCI curve, indicating that amplitude-based selection effectively identifies the physically relevant sector of the Hilbert space. However, the slope of the NQS curve becomes shallower than that of HCI as the subspace size increases. This divergence reflects the methodological difference between the two approaches: HCI performs an exact diagonalization within the selected subspace, whereas NQS relies on non-linear parameter optimization. In high-dimensional subspaces, the optimization may terminate with a non-zero residual vector within the variational manifold.

This optimization residual is quantified by the internal PT2 correction,  $\Delta E_{\text{PT2, internal}}$ . For System II, the magnitude of this correction increases from  $2.49 \times 10^{-5}$  Ha at  $|\mathcal{V}| = 32,768$  to  $1.98 \times 10^{-3}$  Ha at  $|\mathcal{V}| = 1,048,576$ . While the post-optimization PT2 step corrects for this residual, the remaining energy difference relative to the HCI reference is attributable to the combination of this optimization error and the screening threshold ( $\epsilon_{\text{HB}}$ ) applied to the perturbative set  $\mathcal{P}$ .

## 4.5 Computational Efficiency and Complexity Analysis

We analyze the scaling performance of the deterministic framework by decomposing the total wall-time into three computational phases: (1) *Compilation* (Orange): Construction of the sparse Hamiltonian graph and connected set  $\mathcal{C}$  via the C++ kernel; (2) *Inner Loop* (Blue): JAX-compiled optimization steps, performing wavefunction evaluation and gradient accumulation on the GPU; (3) *Overhead* (Green): Subspace management tasks, including candidate scoring, sorting, and host-device data transfer. Figure 4 details the time decomposition for H<sub>2</sub>O, N<sub>2</sub>, and Cr<sub>2</sub> active spaces as a function of the variational set size  $|\mathcal{V}|$ .

The total wall-time follows a power law scaling  $T \propto |\mathcal{V}|^\alpha$  across all benchmarked systems, with exponents ranging from  $\alpha = 0.75$  to  $\alpha = 0.88$ . This sub-linear scaling indicates that the marginal computational

Table 3: Ground-state energies of the  $\text{Cr}_2$  dimer in different active spaces. All energies are reported as  $E + 2086 \text{ Ha}$ .

Method	$ \mathcal{V} $	Variational Energy	Total Energy
<i>System I: CAS(24e, 30o), <math> H  \approx 7.48 \times 10^{15}</math></i>			
CCSDTQ [53]	-	-	-0.406 696
<b>This work</b>	8 192	-0.339 793	-0.418 002
<b>This work</b>	32 768	-0.372 492	-0.417 737
SC-RBM [38]	174 963	-0.383 96	-0.416 920
SC-RBM [38]	385 554	-0.387 52	-0.416 310
HCI [52]	123 144	-0.387 661	-0.420 094
<b>This work</b>	131 072	-0.392 029	-0.419 212
<b>This work</b>	524 288	-0.402 847	-0.419 550
HCI [52]	480 138	-0.402 856	-0.420 541
<b>This work</b>	1 048 576	-0.406 173	-0.420 278
HCI [52]	66 679 956	-0.420 114	-0.421 375
DMRG [54]	-	-0.420 525	-0.421 156
FCIQMC [55]	-	-	-0.421 200
<i>System II: CAS(48e, 42o), <math> H  \approx 1.25 \times 10^{23}</math></i>			
CCSDTQ [53]	-	-	-0.430 244
<b>This work</b>	8 192	-0.330 898	-0.437 190
<b>This work</b>	32 768	-0.381 646	-0.440 195
SC-RBM [38]	156 594	-0.389 78	-0.437 530
SC-RBM [38]	331 397	-0.392 03	-0.434 520
SC-Transformer [36]	-	-0.400 43	-
HCI [52]	190 937	-0.405 000	-0.442 899
<b>This work</b>	131 072	-0.405 377	-0.441 221
<b>This work</b>	524 288	-0.418 717	-0.442 491
HCI [52]	787 919	-0.422 163	-0.443 463
<b>This work</b>	1 048 576	-0.422 971	-0.442 491
HCI [52]	2 237 828	-0.430 093	-0.443 908
HCI [52]	148 589 206	-0.442 773	-0.444 560
DMRG [53]	-	-0.443 334	-0.444 478

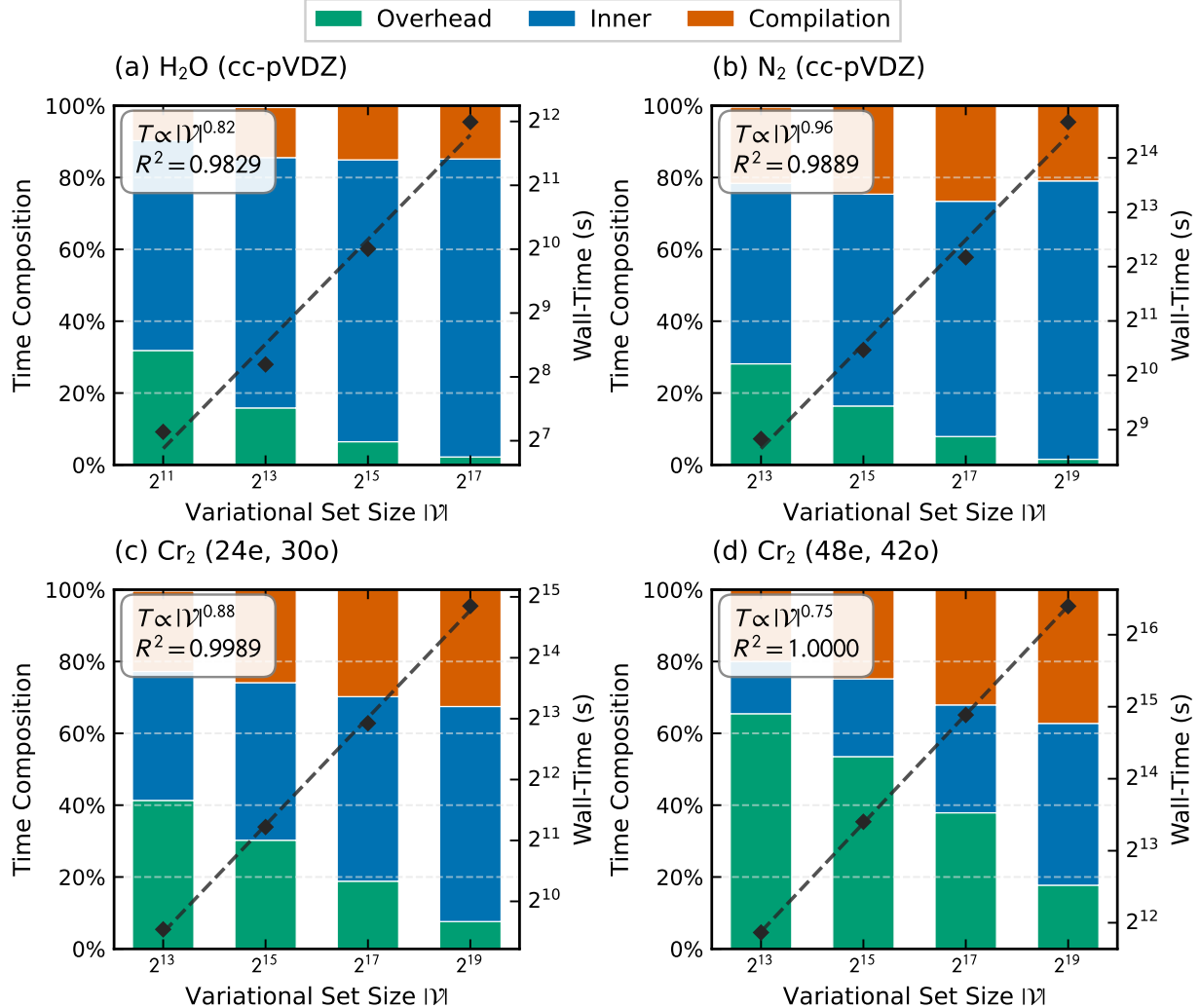


Figure 4: Wall-time decomposition of a single outer-loop iteration versus the variational set size  $|\mathcal{V}|$  for (a)  $\text{H}_2\text{O}$ , (b)  $\text{N}_2$ , (c)  $\text{Cr}_2$  (24e, 30o), and (d)  $\text{Cr}_2$  (48e, 42o). The stacked bars (left axis) represent the relative percentage of each computational phase, while the diamond markers (right axis) track the total wall-time in seconds. The total scaling follows a power law  $T \propto |\mathcal{V}|^\alpha$ , with fitted exponents  $\alpha$  provided in the insets.

cost per configuration decreases as the subspace expands, reflecting the efficiency of batched operations on large datasets. However, the distribution of computational effort depends heavily on the electronic structure complexity.

For the H<sub>2</sub>O and N<sub>2</sub> systems (Figure 4a-b), the workflow is compute-bound. The *Inner Loop* dominates the total runtime (50–80%), as the sparse Hamiltonian graph remains relatively compact. In this regime, performance is limited primarily by the arithmetic intensity of the neural network inference and the GPU memory bandwidth during gradient accumulation.

In contrast, the strongly correlated Cr<sub>2</sub> system (Figure 4c-d) exhibits a different profile due to the dense connectivity of the active space. For the large CAS(48e, 42o), the *Overhead* and *Compilation* phases constitute the majority of the wall-time at small subspace sizes (> 60% at  $|\mathcal{V}| = 2^{13}$ ). This behavior occurs because the size of the connected set  $|\mathcal{C}|$  scales rapidly with the number of open shells, making the CPU-based integer logic for graph generation and screening the primary bottleneck.

As  $|\mathcal{V}|$  increases, however, the relative contribution of the *Inner Loop* rises (e.g., to  $\sim 40\%$  in Figure 4d). This trend suggests that the algorithmic overhead for subspace management effectively saturates, shifting the workload back towards the highly parallelizable GPU operations in the large-scale limit. Additionally, the *Compilation* time remains controlled despite the massive Hilbert space, confirming that the heat-bath screening efficiently prunes the Hamiltonian connectivity graph. The observed scaling exponents ( $\alpha < 0.9$ ) demonstrate that the hybrid architecture successfully balances discrete combinatorial logic on the host with differentiable linear algebra on the device, maintaining tractability for variational sets exceeding  $10^5$  configurations.

## 5 Conclusion and Outlook

We have presented a deterministic optimization framework for NQS, reformulating the electronic Schrödinger equation as a non-linear optimization problem over dynamically adaptive configuration subspaces. By replacing stochastic gradient estimation with exact summation within a variational set, this approach eliminates the sampling noise and slow mixing associated with MCMC in discrete Fock spaces. Our results demonstrate that optimizing the ansatz within a variational set ( $\mathcal{V}$ ), combined with a PT2 correction, effectively captures both static and dynamic correlations.

Benchmarks on small molecules and bond dissociations show that the method recovers the static correlation and dynamic correlation, avoiding the failures common in single-reference Coupled Cluster methods. For the strongly correlated Cr<sub>2</sub> in large active spaces [CAS(48e, 42o)], the framework maintains accuracy comparable to the sCI references while exhibiting sub-linear wall-time scaling with respect to the set size

$(T \propto |\mathcal{V}|^\alpha, \alpha < 1)$ . These findings indicate that neural backflow ansätze can efficiently approximate complex wavefunctions in Hilbert spaces exceeding  $10^{23}$ , provided the dominant amplitudes are localized within a treatable subspace.

However, the current time-to-solution remains higher than mature sCI and DMRG solvers. The primary bottleneck lies in the high arithmetic intensity of neural network tensor contractions compared to the optimized sparse matrix-vector products used in linear CI methods. Additionally, the efficiency of deterministic subspace expansion relies on the sparsity of the ground state in the chosen orbital basis. For systems with dense entanglement or significant delocalization, the rapid growth of the required variational support  $|\mathcal{V}|$  may diminish the computational advantages of this formulation.

Future work will address these limitations through the following extensions:

- **Orbital Optimization:** As sparsity is basis-dependent, integrating orbital optimization (e.g., via simultaneous gradient updates) is necessary to minimize the variational set size  $|\mathcal{V}|$  required for target accuracy, thereby compacting the wavefunction representation[56, 57].
- **Symmetry Adaptation:** The current ansatz implies but does not strictly enforce total spin ( $S^2$ ) or point-group symmetries. Explicitly incorporating these constraints via symmetry-projected networks or penalty functions will reduce spin contamination, particularly in open-shell transition metals[26, 58].
- **Advanced Ansatz Architectures:** While the MLP backflow provides a generic baseline, future work can explore architectures with stronger physical priors or higher expressivity. This includes incorporating explicit physical constraints via Pfaffian and Jastrow structures, or hybrid Neuro-Tensor Network states to improve data efficiency[59–62]. Furthermore, integrating geometry-aware architectures, such as Graph Neural Networks, or leveraging the long-range dependency modeling of Transformers, could enhance the capture of non-local correlations in larger basis sets[23, 63].
- **Optimization Algorithms and Strategies:** The availability of noise-free gradients within the deterministic framework facilitates the application of advanced optimization techniques to address ill-conditioned curvature. This includes curvature-aware algorithms such as exact SR and its low-rank variants (e.g., minSR)[31, 64, 65]. Additionally, the absence of sampling variance allows for precise gradient-based convergence control and dynamic optimization strategies, such as adaptive learning rate scheduling and automated hyperparameter stepping.
- **Hybrid Deterministic-Stochastic Schemes:** To recover dynamic correlation from the vast perturbative set without excessive memory costs, a hybrid approach may be employed[37, 66]. This would

combine deterministic optimization of the strongly correlated core with stochastic sampling of the perturbative tail, balancing variational rigor with the scalability of Monte Carlo integration.

In summary, this framework formulates NQS optimization within a rigorous linear algebra context, treating the network as a differentiable function approximator rather than a probability sampler. By decoupling ansatz design from sampling challenges, it offers a distinct pathway for applying deep learning to high-precision ab initio quantum chemistry.

## Acknowledgements

The author thanks the Supercomputing Center of the University of Science and Technology of China for providing the computational resources used in this work. The author is also grateful to Qiang Fu for helpful discussions and support. The NetKet codebase is acknowledged as a learning and inspiration resource for the development of the software framework used in this study [67, 68]. Additionally, the author acknowledges the use of generative AI for language polishing and text refinement to improve the clarity and readability of the manuscript.

## Code Availability

The source code for the deterministic NQS framework, including the hybrid CPU-GPU implementation and example scripts, is publicly available on GitHub at <https://github.com/wsmxcz/DetNQS>. This repository also contains the molecular Hamiltonian integrals (in FCIDUMP format) used for the benchmarks presented in this study.

## Data Availability

The data that support the findings of this study, including molecular geometries, and detailed energy results, are available within the article and its Supporting Information. Any additional raw data are available from the corresponding author upon reasonable request.

## References

- (1) Sherrill, C. D.; Schaefer III, H. F. In *Advances in Quantum Chemistry*; Elsevier: 1999; Vol. 34, pp 143–269, DOI: [10.1016/S0065-3276\(08\)60532-8](https://doi.org/10.1016/S0065-3276(08)60532-8).

(2) Helgaker, T.; Jørgensen, P.; Olsen, J., *Molecular Electronic-Structure Theory*; John Wiley & Sons: Chichester, U.K., 2013.

(3) Szabo, A.; Ostlund, N. S., *Modern Quantum Chemistry: Introduction to Advanced Electronic Structure Theory*; Dover Publications: Mineola, NY, 2012.

(4) Huron, B.; Malrieu, J.-P.; Rancurel, P. Iterative Perturbation Calculations of Ground and Excited State Energies from Multiconfigurational Zeroth-Order Wavefunctions. *The Journal of Chemical Physics* **1973**, *58*, 5745–5759, DOI: [10.1063/1.1679199](https://doi.org/10.1063/1.1679199).

(5) Holmes, A. A.; Tubman, N. M.; Umrigar, C. J. Heat-Bath Configuration Interaction: An Efficient Selected Configuration Interaction Algorithm Inspired by Heat-Bath Sampling. *Journal of Chemical Theory and Computation* **2016**, *12*, 3674–3680, DOI: [10.1021/acs.jctc.6b00407](https://doi.org/10.1021/acs.jctc.6b00407).

(6) Tubman, N. M.; Freeman, C. D.; Levine, D. S.; Hait, D.; Head-Gordon, M.; Whaley, K. B. Modern Approaches to Exact Diagonalization and Selected Configuration Interaction with the Adaptive Sampling CI Method. *Journal of Chemical Theory and Computation* **2020**, *16*, 2139–2159, DOI: [10.1021/acs.jctc.8b00536](https://doi.org/10.1021/acs.jctc.8b00536).

(7) Zhang, N.; Liu, W.; Hoffmann, M. R. Iterative Configuration Interaction with Selection. *Journal of Chemical Theory and Computation* **2020**, *16*, 2296–2316, DOI: [10.1021/acs.jctc.9b01200](https://doi.org/10.1021/acs.jctc.9b01200).

(8) Raghavachari, K.; Trucks, G. W.; Pople, J. A.; Head-Gordon, M. A Fifth-Order Perturbation Comparison of Electron Correlation Theories. *Chemical Physics Letters* **1989**, *157*, 479–483, DOI: [10.1016/S0009-2614\(89\)87395-6](https://doi.org/10.1016/S0009-2614(89)87395-6).

(9) Bartlett, R. J.; Musiał, M. Coupled-Cluster Theory in Quantum Chemistry. *Reviews of Modern Physics* **2007**, *79*, 291–352, DOI: [10.1103/RevModPhys.79.291](https://doi.org/10.1103/RevModPhys.79.291).

(10) White, S. R.; Martin, R. L. *Ab initio* Quantum Chemistry Using the Density Matrix Renormalization Group. *The Journal of Chemical Physics* **1999**, *110*, 4127–4130, DOI: [10.1063/1.478295](https://doi.org/10.1063/1.478295).

(11) Chan, G. K.-L.; Sharma, S. The Density Matrix Renormalization Group in Quantum Chemistry. *Annual Review of Physical Chemistry* **2011**, *62*, 465–481, DOI: [10.1146/annurev-physchem-032210-103338](https://doi.org/10.1146/annurev-physchem-032210-103338).

(12) Carleo, G.; Troyer, M. Solving the Quantum Many-Body Problem with Artificial Neural Networks. *Science* **2017**, *355*, 602–606, DOI: [10.1126/science.aag2302](https://doi.org/10.1126/science.aag2302).

(13) Deng, D.-L.; Li, X.; Das Sarma, S. Quantum Entanglement in Neural Network States. *Physical Review X* **2017**, *7*, 021021, DOI: [10.1103/PhysRevX.7.021021](https://doi.org/10.1103/PhysRevX.7.021021).

(14) Choo, K.; Mezzacapo, A.; Carleo, G. Fermionic Neural-Network States for *ab-initio* Electronic Structure. *Nature Communications* **2020**, *11*, 2368, DOI: [10.1038/s41467-020-15724-9](https://doi.org/10.1038/s41467-020-15724-9).

(15) Sharir, O.; Shashua, A.; Carleo, G. Neural Tensor Contractions and the Expressive Power of Deep Neural Quantum States. *Physical Review B* **2022**, *106*, 205136, DOI: [10.1103/PhysRevB.106.205136](https://doi.org/10.1103/PhysRevB.106.205136).

(16) Medvidović, M.; Moreno, J. R. Neural-network Quantum States for Many-Body Physics. *The European Physical Journal Plus* **2024**, *139*, 638, DOI: [10.1140/epjp/s13360-024-05311-y](https://doi.org/10.1140/epjp/s13360-024-05311-y).

(17) Lange, H.; Van de Walle, A.; Abedinnia, A.; Bohrdt, A. From Architectures to Applications: A Review of Neural Quantum States. *Quantum Science and Technology* **2024**, *9*, 032001, DOI: [10.1088/2058-9565/ad7168](https://doi.org/10.1088/2058-9565/ad7168).

(18) Hermann, J.; Spencer, J.; Choo, K.; Mezzacapo, A.; Foulkes, W. M. C.; Pfau, D.; Carleo, G.; Noé, F. *Ab Initio* Quantum Chemistry with Neural-Network Wavefunctions. *Nature Reviews Chemistry* **2023**, *7*, 692–709, DOI: [10.1038/s41570-023-00516-8](https://doi.org/10.1038/s41570-023-00516-8).

(19) Hermann, J.; Schätzle, Z.; Noé, F. Deep-Neural-Network Solution of the Electronic Schrödinger Equation. *Nature Chemistry* **2020**, *12*, 891–897, DOI: [10.1038/s41557-020-0544-y](https://doi.org/10.1038/s41557-020-0544-y).

(20) Pfau, D.; Spencer, J. S.; Matthews, A. G. D. G.; Foulkes, W. M. C. *Ab initio* Solution of the Many-Electron Schrödinger Equation with Deep Neural Networks. *Physical Review Research* **2020**, *2*, 033429, DOI: [10.1103/PhysRevResearch.2.033429](https://doi.org/10.1103/PhysRevResearch.2.033429).

(21) Li, X.; Huang, J.-C.; Zhang, G.-Z.; Li, H.-E.; Cao, C.-S.; Lv, D.; Hu, H.-S. A Nonstochastic Optimization Algorithm for Neural-Network Quantum States. *Journal of Chemical Theory and Computation* **2023**, *19*, 8156–8165, DOI: [10.1021/acs.jctc.3c00831](https://doi.org/10.1021/acs.jctc.3c00831).

(22) Liu, A.-J.; Clark, B. K. Neural Network Backflow for *ab initio* Quantum Chemistry. *Physical Review B* **2024**, *110*, 115137, DOI: [10.1103/PhysRevB.110.115137](https://doi.org/10.1103/PhysRevB.110.115137).

(23) Shang, H.; Guo, C.; Wu, Y.; Li, Z.; Yang, J. Solving the Many-Electron Schrödinger Equation with a Transformer-Based Framework. *Nature Communications* **2025**, *16*, 8464, DOI: [10.1038/s41467-025-63219-2](https://doi.org/10.1038/s41467-025-63219-2).

(24) Sharir, O.; Levine, Y.; Wies, N.; Carleo, G.; Shashua, A. Deep Autoregressive Models for the Efficient Variational Simulation of Many-Body Quantum Systems. *Physical Review Letters* **2020**, *124*, 020503, DOI: [10.1103/PhysRevLett.124.020503](https://doi.org/10.1103/PhysRevLett.124.020503).

(25) Barrett, T. D.; Malyshev, A.; Lvovsky, A. I. Autoregressive Neural-Network Wavefunctions for *ab initio* Quantum Chemistry. *Nature Machine Intelligence* **2022**, *4*, 351–358, DOI: [10.1038/s42256-022-00461-z](https://doi.org/10.1038/s42256-022-00461-z).

(26) Luo, D.; Chen, Z.; Hu, K.; Zhao, Z.; Hur, V. M.; Clark, B. K. Gauge-Invariant and Anyonic-Symmetric Autoregressive Neural Network for Quantum Lattice Models. *Physical Review Research* **2023**, *5*, 013216, DOI: [10.1103/PhysRevResearch.5.013216](https://doi.org/10.1103/PhysRevResearch.5.013216).

(27) Ibarra-García-Padilla, E.; Lange, H.; Melko, R. G.; Scalettar, R. T.; Carrasquilla, J.; Bohrdt, A.; Khatami, E. Autoregressive Neural Quantum States of Fermi-Hubbard Models. *Physical Review Research* **2025**, *7*, 013122, DOI: [10.1103/PhysRevResearch.7.013122](https://doi.org/10.1103/PhysRevResearch.7.013122).

(28) Kan, B.; Shang, H. Accelerating Many-Body Quantum Chemistry via Generative Transformer-Enhanced Configuration Interaction. *Journal of Chemical Theory and Computation* **2025**, *21*, 11989–12000, DOI: [10.1021/acs.jctc.5c01429](https://doi.org/10.1021/acs.jctc.5c01429).

(29) Coe, J. P. Machine Learning Configuration Interaction. *Journal of Chemical Theory and Computation* **2018**, *14*, 5739–5749, DOI: [10.1021/acs.jctc.8b00849](https://doi.org/10.1021/acs.jctc.8b00849).

(30) Wang, J.-Q.; Wu, H.-Q.; He, R.-Q.; Lu, Z.-Y. Variational Optimization of the Amplitude of Neural-Network Quantum Many-Body Ground States. *Physical Review B* **2024**, *109*, 245120, DOI: [10.1103/PhysRevB.109.245120](https://doi.org/10.1103/PhysRevB.109.245120).

(31) Sorella, S. Green Function Monte Carlo with Stochastic Reconfiguration. *Physical Review Letters* **1998**, *80*, 4558–4561, DOI: [10.1103/PhysRevLett.80.4558](https://doi.org/10.1103/PhysRevLett.80.4558).

(32) Park, C.-Y.; Kastoryano, M. J. Geometry of Learning Neural Quantum States. *Physical Review Research* **2020**, *2*, 023232, DOI: [10.1103/PhysRevResearch.2.023232](https://doi.org/10.1103/PhysRevResearch.2.023232).

(33) Nomura, Y.; Darmawan, A. S.; Yamaji, Y.; Imada, M. Restricted Boltzmann Machine Learning for Solving Strongly Correlated Quantum Systems. *Physical Review B* **2017**, *96*, 205152, DOI: [10.1103/PhysRevB.96.205152](https://doi.org/10.1103/PhysRevB.96.205152).

(34) Humeniuk, S.; Wan, Y.; Wang, L. Autoregressive Neural Slater-Jastrow Ansatz for Variational Monte Carlo Simulation. *SciPost Physics* **2023**, *14*, 171, DOI: [10.21468/SciPostPhys.14.6.171](https://doi.org/10.21468/SciPostPhys.14.6.171).

(35) Luo, D.; Clark, B. K. Backflow Transformations via Neural Networks for Quantum Many-Body Wave Functions. *Physical Review Letters* **2019**, *122*, 226401, DOI: [10.1103/PhysRevLett.122.226401](https://doi.org/10.1103/PhysRevLett.122.226401).

(36) Kan, B.; Zhou, Y.; Xie, D.; Zhou, P.; Zhang, Y.; Shang, H. In *Proceedings of the International Conference for High Performance Computing, Networking, Storage and Analysis*, 2025, pp 1646–1660, DOI: [10.1145/3712285.3759800](https://doi.org/10.1145/3712285.3759800).

(37) Liu, A.-J.; Clark, B. K. Efficient Optimization of Neural Network Backflow for *ab initio* Quantum Chemistry. *Physical Review B* **2025**, *112*, 155162, DOI: [10.1103/thz7-1mdn](https://doi.org/10.1103/thz7-1mdn).

(38) Li, X.; Huang, J.-C.; Zhang, G.-Z.; Li, H.-E.; Shen, Z.-P.; Zhao, C.; Li, J.; Hu, H.-S. Improved Optimization for the Neural-Network Quantum States and Tests on the Chromium Dimer. *The Journal of Chemical Physics* **2024**, *160*, 234105, DOI: [10.1063/5.0214150](https://doi.org/10.1063/5.0214150).

(39) Sharma, S. Stochastic Perturbation Theory to Correct Non-linearly Parametrized Wavefunctions. *arXiv preprint arXiv:1803.04341* **2018**.

(40) Jakob, W. nanobind: Tiny and Efficient C++/Python Bindings, <https://github.com/wjakob/nanobind>, 2022.

(41) Bradbury, J. et al. JAX: Composable Transformations of Python+NumPy Programs, version 0.8.2, 2018.

(42) Virtanen, P.; Gommers, R.; Oliphant, T. E.; Haberland, M.; Reddy, T.; Cournapeau, D.; Burovski, E.; Peterson, P.; Weckesser, W.; Bright, J., et al. SciPy 1.0: Fundamental Algorithms for Scientific Computing in Python. *Nature Methods* **2020**, *17*, 261–272, DOI: [10.1038/s41592-019-0686-2](https://doi.org/10.1038/s41592-019-0686-2).

(43) Holmes, A. A.; Changlani, H. J.; Umrigar, C. J. Efficient Heat-Bath Sampling in Fock Space. *Journal of Chemical Theory and Computation* **2016**, *12*, 1561–1571, DOI: [10.1021/acs.jctc.5b01170](https://doi.org/10.1021/acs.jctc.5b01170).

(44) Sun, Q.; Berkelbach, T. C.; Blunt, N. S.; Booth, G. H.; Guo, S.; Li, Z.; Liu, J.; McClain, J. D.; Sayfutyarova, E. R.; Sharma, S., et al. PySCF: The Python-based Simulations of Chemistry Framework. *Wiley Interdisciplinary Reviews: Computational Molecular Science* **2018**, *8*, e1340, DOI: [10.1002/wcms.1340](https://doi.org/10.1002/wcms.1340).

(45) Sun, Q.; Zhang, X.; Banerjee, S.; Bao, P.; Barbry, M.; Blunt, N. S.; Bogdanov, N. A.; Booth, G. H.; Chen, J.; Cui, Z.-H., et al. Recent Developments in the PySCF Program Package. *The Journal of Chemical Physics* **2020**, *153*, 024112, DOI: [10.1063/5.0006074](https://doi.org/10.1063/5.0006074).

(46) Sun, Q. Libcint: An Efficient General Integral Library for Gaussian Basis Functions. *Journal of Computational Chemistry* **2015**, *36*, 1664–1671, DOI: [10.1002/jcc.23981](https://doi.org/10.1002/jcc.23981).

(47) Zhao, T.; Stokes, J.; Veerapaneni, S. Scalable Neural Quantum States Architecture for Quantum Chemistry. *Machine Learning: Science and Technology* **2023**, *4*, 025034, DOI: [10.1088/2632-2153/acdb2f](https://doi.org/10.1088/2632-2153/acdb2f).

(48) Gao, H.; Imamura, S.; Kasagi, A.; Yoshida, E. Distributed Implementation of Full Configuration Interaction for One Trillion Determinants. *Journal of Chemical Theory and Computation* **2024**, *20*, 1185–1192, DOI: [10.1021/acs.jctc.3c01190](https://doi.org/10.1021/acs.jctc.3c01190).

(49) Olsen, J.; Jørgensen, P.; Koch, H.; Balkova, A.; Bartlett, R. J. Full Configuration–Interaction and State of the Art Correlation Calculations on Water in a Valence Double-Zeta Basis with Polarization Functions. *The Journal of Chemical Physics* **1996**, *104*, 8007–8015, DOI: [10.1063/1.471518](https://doi.org/10.1063/1.471518).

(50) Chan, G. K.-L.; Kállay, M.; Gauss, J. State-of-the-art Density Matrix Renormalization Group and Coupled Cluster Theory Studies of the Nitrogen Binding Curve. *The Journal of Chemical Physics* **2004**, *121*, 6110–6116, DOI: [10.1063/1.1783212](https://doi.org/10.1063/1.1783212).

(51) Wang, Z.; Li, Y.; Lu, J. Coordinate Descent Full Configuration Interaction. *Journal of Chemical Theory and Computation* **2019**, *15*, 3558–3569, DOI: [10.1021/acs.jctc.9b00138](https://doi.org/10.1021/acs.jctc.9b00138).

(52) Li, J.; Yao, Y.; Holmes, A. A.; Otten, M.; Sun, Q.; Sharma, S.; Umrigar, C. J. Accurate Many-Body Electronic Structure Near the Basis Set Limit: Application to the Chromium Dimer. *Physical Review Research* **2020**, *2*, 012015, DOI: [10.1103/PhysRevResearch.2.012015](https://doi.org/10.1103/PhysRevResearch.2.012015).

(53) Olivares-Amaya, R.; Hu, W.; Nakatani, N.; Sharma, S.; Yang, J.; Chan, G. K.-L. The *ab initio* Density Matrix Renormalization Group in Practice. *The Journal of Chemical Physics* **2015**, *142*, 034102, DOI: [10.1063/1.4905329](https://doi.org/10.1063/1.4905329).

(54) Sharma, S.; Chan, G. K.-L. Spin-Adapted Density Matrix Renormalization Group Algorithms for Quantum Chemistry. *The Journal of Chemical Physics* **2012**, *136*, 124121, DOI: [10.1063/1.3695642](https://doi.org/10.1063/1.3695642).

(55) Booth, G. H.; Smart, S. D.; Alavi, A. Linear-Scaling and Parallelisable Algorithms for Stochastic Quantum Chemistry. *Molecular Physics* **2014**, *112*, 1855–1869, DOI: [10.1080/00268976.2013.877165](https://doi.org/10.1080/00268976.2013.877165).

(56) Smith, J. E. T.; Mussard, B.; Holmes, A. A.; Sharma, S. Cheap and Near Exact CASSCF with Large Active Spaces. *Journal of Chemical Theory and Computation* **2017**, *13*, 5468–5478, DOI: [10.1021/acs.jctc.7b00900](https://doi.org/10.1021/acs.jctc.7b00900).

(57) Yao, Y.; Umrigar, C. J. Orbital Optimization in Selected Configuration Interaction Methods. *Journal of Chemical Theory and Computation* **2021**, *17*, 4183–4194, DOI: [10.1021/acs.jctc.1c00385](https://doi.org/10.1021/acs.jctc.1c00385).

(58) Jiménez-Hoyos, C. A.; Henderson, T. M.; Tsuchimochi, T.; Scuseria, G. E. Projected Hartree–Fock Theory. *The Journal of Chemical Physics* **2012**, *136*, 164109, DOI: [10.1063/1.4705280](https://doi.org/10.1063/1.4705280).

(59) Chen, A.; Wan, Z.-Q.; Sengupta, A.; Georges, A.; Roth, C. Neural Network-Augmented Pfaffian Wave-Functions for Scalable Simulations of Interacting Fermions. *arXiv preprint arXiv:2507.10705* **2025**.

(60) Wu, Z.; Zhang, B.; Fang, W.-H.; Li, Z. Hybrid Tensor Network and Neural Network Quantum States for Quantum Chemistry. *Journal of Chemical Theory and Computation* **2025**, *21*, 10252–10262, DOI: [10.1021/acs.jctc.5c01228](https://doi.org/10.1021/acs.jctc.5c01228).

(61) Du, S.-J.; Chen, A.; Chan, G. K.-L. Neuralized Fermionic Tensor Networks for Quantum Many-Body Systems. *arXiv preprint arXiv:2506.08329* **2025**.

(62) Li, Z.; Zhao, T.; Zhang, B. Representational power of selected neural network quantum states in second quantization. *arXiv preprint arXiv:2511.04932* **2025**.

(63) Liang, X.; Dong, S.-J.; He, L. Hybrid Convolutional Neural Network and Projected Entangled Pair States Wave Functions for Quantum Many-Particle States. *Physical Review B* **2021**, *103*, 035138, DOI: [10.1103/PhysRevB.103.035138](https://doi.org/10.1103/PhysRevB.103.035138).

(64) Sorella, S. Generalized Lanczos Algorithm for Variational Quantum Monte Carlo. *Physical Review B* **2001**, *64*, 024512, DOI: [10.1103/PhysRevB.64.024512](https://doi.org/10.1103/PhysRevB.64.024512).

(65) Chen, A.; Heyl, M. Empowering Deep Neural Quantum States through Efficient Optimization. *Nature Physics* **2024**, *20*, 1476–1481, DOI: [10.1038/s41567-024-02566-1](https://doi.org/10.1038/s41567-024-02566-1).

(66) Sharma, S.; Holmes, A. A.; Jeanmairet, G.; Alavi, A.; Umrigar, C. J. Semistochastic Heat-Bath Configuration Interaction Method: Selected Configuration Interaction with Semistochastic Perturbation Theory. *Journal of Chemical Theory and Computation* **2017**, *13*, 1595–1604, DOI: [10.1021/acs.jctc.6b01028](https://doi.org/10.1021/acs.jctc.6b01028).

(67) Vicentini, F. et al. NetKet 3: Machine Learning Toolbox for Many-Body Quantum Systems. *SciPost Physics Codebases* **2022**, *7*, DOI: [10.21468/SciPostPhysCodeb.7](https://doi.org/10.21468/SciPostPhysCodeb.7).

(68) Carleo, G. et al. NetKet: A Machine Learning Toolkit for Many-Body Quantum Systems. *SoftwareX* **2019**, *10*, 100311, DOI: [10.1016/j.softx.2019.100311](https://doi.org/10.1016/j.softx.2019.100311).